Riverine organic matter dynamics in the headwaters of the Yellow River under climate change

Xiaoxiao Wang [1,2], Jie Wang [1], Tianqing Ren [1], and Jun Zhou [3]

[1] School of Geographical Sciences, China West Normal University, Nanchong 637009, China

[2] Sichuan Provincial Engineering Research Center of Monitoring and Control for Soil Erosion in Dry Valleys, China West Normal University, Nanchong 637009, China

[3] Institute of Mountain Hazards and Environment, Chinese Academy of Sciences, Chengdu 610213, China

Correspondence to: Xiaoxiao Wang (wxx1989@cwnu.edu.cn)

Xiaoxiao Wang and Jie Wang contributed equally to this work.

Abstract: Alpine headwater streams play a crucial role in the global carbon cycle and are particularly sensitive to climate change. Riverine organic matter (ROM) mediates the transport and transformation of terrestrial carbon across aquatic systems. However, how ROM responds to climate change in the headwaters of the Qinghai-Tibetan Plateau (QTP) remains poorly understood, largely owing to a lack of long-term, high-spatial-resolution in-situ measurements. In this study, we used machine learning models combining satellite data and geographical variables to reconstruct historical variations in Chemical Oxygen Demand (COD_{Mn}, a proxy for ROM) along the Yellow River's Headstream (YRHS), and to predict future changes under typical Shared Socioeconomic Pathways. The results indicate that COD_{Mn} levels in the midstream region of the YRHS, characterized by greater precipitation, higher soil organic matter, and denser vegetation, were relatively high (2.73 ± 1.63 mg L^{-1}) and exhibited an increasing trend (0.58 mg L^{-1}) over the past decade. Driven primarily by increasing precipitation and temperature, COD_{Mn} levels are projected to rise in upstream and downstream areas but decline at midstream sites under SSP126, SSP245, and SSP585 by 2100. The annual export of riverine organic matter from the midstream of the YRHS is expected to remain stable by 2100. Therefore, our findings identify the midstream region of the YRHS as a critical and climate-sensitive region for organic matter dynamics. Though our study provides a comprehensive understanding of how climate change is reshaping riverine organic matter dynamics, substantial uncertainties remain in the future riverine organic matter changes owing to the complex interactions among precipitation, warming, hydrology and their combined effects on carbon cycles in alpine catchments.

Key words: Alpine River; Carbon cycle; Climate change; Remote sensing; Qinghai–Tibetan Plateau

1 Introduction

Alpine regions represent some of the most vulnerable ecosystems to climate change, experiencing temperature increases nearly twice the global average (Kotlarski et al., 2023; Aryal and Pokhrel, 2025). Among them, the Qinghai–Tibetan Plateau (QTP), often referred to as the “Third Pole”, is the highest and one of the most climate-sensitive regions on Earth (Chen et al., 2022; Wang et al., 2023). In recent decades, the accelerated warming has triggered widespread environmental changes on the QTP, which are expected to significantly alter the sources, forms, and fluxes of carbon exports associated with permafrost degradation (Chen et al., 2022; Xu et al., 2024; Hong et al., 2025). Studies have shown that parts of the QTP have already shifted from carbon sinks to carbon sources and lateral transport of carbon has increased the riverine carbon fluxes on the QTP (Li et al., 2025). Riverine organic matter (ROM) plays a pivotal role in the biogeochemical cycles of carbon (Hu et al., 2020; Giri, 2021; Regnier et al., 2022; Beusen et al., 2022), and the increase in ROM will pose threats to the water quality of rivers on the QTP. Despite growing concern regarding the ROM and its ecological consequences, our understanding of ROM dynamics across the QTP remains limited. Therefore, there is an urgent need for high spatial resolution and long-term observations of ROM dynamics and their exports on the QTP.

Headwater streams account for approximately 61% of total riverine carbon efflux despite representing only 34–38% of total stream surface area (Li et al., 2021). Over recent decades, climate change has substantially influenced the carbon dynamics of headstreams on the QTP (Yao et al., 2022; Li et al., 2025). Long-term records show that the annual streamflow of headstreams in this region has generally increased over the past six decades (1962–2019) (Zhang et al., 2024). Warming and wetting trends have contributed to higher ROM in the headwaters (Xu et al., 2024).

Furthermore, climate-induced changes have intensified sediment erosion and enhanced associated ROM transport processes across the QTP (Zhao et al., 2023; Li et al., 2024, 2025). Nevertheless, fewer than 30% of headstreams across the QTP are consistently monitored (Li et al., 2024), leaving the responses of ROM dynamics in headwaters to climate change poorly constrained.

The limited understanding of ROM dynamics in alpine headwaters is largely due to the scarcity of long-term, continuous in-situ measurements, where data collection remains logistically challenging. In recent years, advances in remote sensing and machine learning have provided powerful alternatives for addressing these limitations, offering new opportunities to predict water quality and infer nutrient-related parameters across extensive spatial and temporal scales (Adegun et al., 2023; Zeng et al., 2023; Zhi et al., 2024). Satellite-derived indices such as reflectance ratios, the Normalized Difference Chlorophyll Index (NDCI), the Suspended Sediment Index (SSI), etc., have been increasingly employed to assess riverine organic matter, particularly when integrated with machine learning algorithms (Liu et al., 2021; Deng et al., 2024; Yan et al., 2025). Consequently, integrating remote sensing data with in-situ measurements and machine learning holds significant potential for improving our understanding of ROM in headwaters and their responses to ongoing climate change.

The Yellow River's headstream (YRHS), located on the eastern QTP, constitute a crucial component of QTP's water resources and carbon cycling systems and have undergone substantial environmental changes in recent decades (Wen et al., 2024). Current study indicated that approximately 35% of the Yellow River's source region serves as a net carbon source, and the lateral transport of carbon accounts for 31% of net ecosystem production in the Yellow River's source region (Li et al., 2025). The YRHS lies in a transition zone between permafrost and

seasonally frozen ground, where climate warming has driven substantial permafrost degradation and triggered a cascade of environmental and ecological issues (Yang et al., 2023). While riverine organic matter dynamics have been extensively studied across the Yellow River Basin (Deng et al., 2025; Lan et al., 2025), the long-term and projected trajectories of ROM in its headwater region have received little attention, which is largely attributable to limited monitoring network coverage in this region. Therefore, given the critical role of the Yellow River headwaters in carbon cycling and downstream water quality and its sensitivity to climate change, there is an urgent need to investigate the dynamics of riverine organic matter in the headwaters of the Yellow River under climate change.

According to previous studies, ROM was estimated using the permanganate index (COD_{Mn}) as a proxy across China (Jiao et al., 2021; Lv et al., 2024; X. Wang et al., 2025; Shang et al., 2026), and significant linear relationships exist between COD_{Mn} and dissolved organic carbon across various aquatic environments (Shang et al., 2026; Wang et al., 2026). Therefore, COD_{Mn} can be used as a proxy for riverine organic matter in the alpine study area. Accordingly, in this study, we focus on the source region of the Yellow River to develop COD_{Mn} predictive models by combining in situ water quality observations with satellite reflectance data and to assess future changes under the SSP126, SSP245, and SSP585 scenarios. The objectives are to: (1) quantify the decadal variability of COD_{Mn} in the headstreams of the Yellow River and identify its driving factors; (2) predict future changes in COD_{Mn} under projected climate change scenarios; and (3) estimate COD_{Mn} exports and assess their potential impacts on downstream ecosystems. This study aims to provide a comprehensive and scalable understanding of how climate change is reshaping riverine organic matter dynamics within one of the world's most critical headwater regions.

2 Methods and materials

2.1 Study area

The source region of the Yellow River is situated in the eastern QTP (Fig. 1a), covering approximately 133,000 km², with elevations ranging from 2650 m to 6250 m. The mean annual temperature in this area ranges between −3.5 and 7.5 °C. The annual average precipitation in this area ranges from 420 to 705 mm, with the highest values occurring in the midstream region (Yang et al., 2023). The dominant land cover consists of alpine meadows and alpine steppes (Fig. S1). The area covers extensive permafrost and seasonally frozen ground, together covering more than 85% of the region (Zongjie Li et al., 2025; Yang et al., 2025). Under the combined influence of climate warming and anthropogenic disturbances, permafrost in the upper reaches of the Yellow River source region has shown a significant trend of degradation in recent decades (Yang et al., 2023). The headwater region of the Yellow River (defined as upstream Xunhua (M4) in this study, which is located on the edge of the Tibetan Plateau) contains a dense network of tributaries with annual average discharge of 1.85×10^{10} m^3 during 1987-2016. Because damming affects the hydrology downstream of Tangnaihai (M2), the discharge at M2 is considered representative of the study area's natural discharge in our study. Within the national surface water quality monitoring network, four sites (M1–M4, Maqu, Tangnaihai, Longyangxia, and Xunhua) are situated at the headwaters of the Yellow River (Fig. 1b). In this study, the upstream (source to Deang), midstream (Deang to Longwu), and downstream sections (Longwu to Xunhua) of the Yellow River's source region are divided based on their geographical characteristics and are labeled B1(source-C1), B2 (C1-C2), and B3 (C2-C3) (Fig. 1).

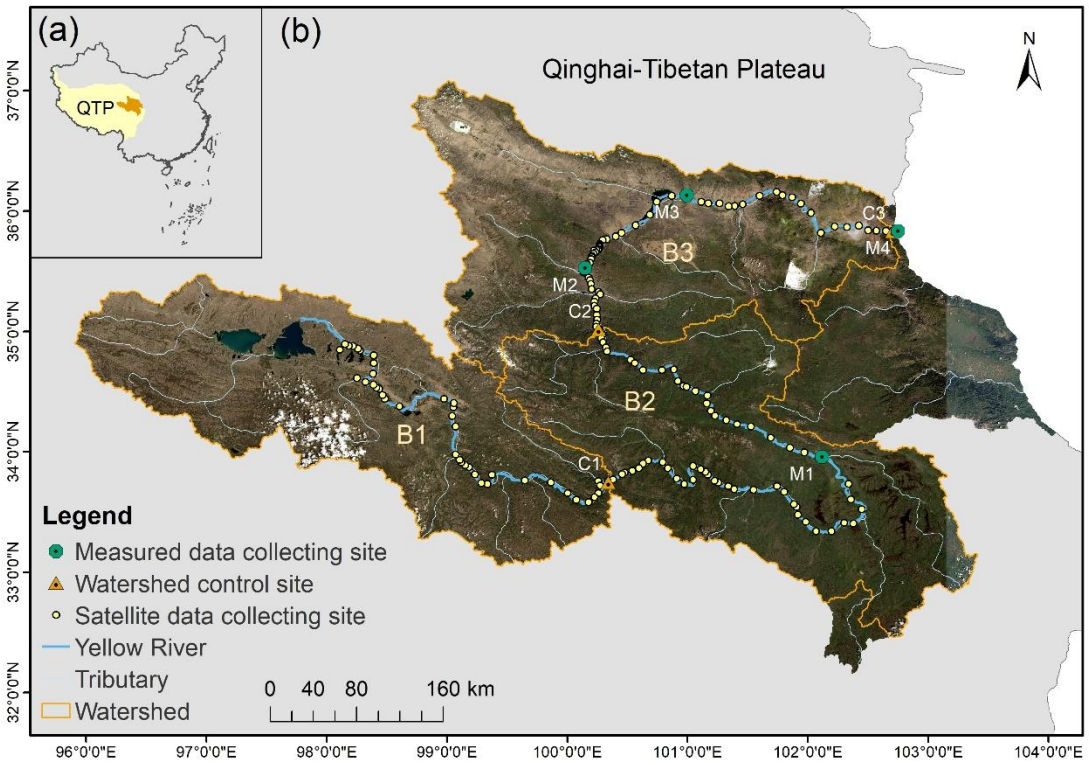


Fig.1 Location of the source region of the Yellow River (a), river network within the study area and data collection sites along the mainstream of the Yellow River (b). B1–B3 represent the upstream (source -C1), midstream (C1-C2), and downstream (C2-C3) region of the Yellow River's headstream in this study. A total of 160 monitoring sites span from downstream to upstream, with Site 1 located at the basin outlet.

2.2 Data collection

2.2.1 In-situ water quality data

Riverine COD_{Mn} data for model training were obtained from 107 monitoring sites distributed across the QTP and surrounding regions (Fig. S2), including four sites (M1–M4) positioned along the mainstream of the Yellow River (Fig. 1b). COD_{Mn} data for each site was obtained from the China National Environmental Monitoring Centre (CNEMC; https://www.cnemc.cn/) for the period 2021–2023. Measurements were performed every four hours (00:00, 04:00, 08:00, 12:00,

16:00, and 20:00). Following the *Environmental Quality Standards for Surface Water* (GB 3838–2002), COD_{Mn} was determined using the acidic potassium permanganate method, in which 50 ml water sample was oxidized by standardized $KMnO_4$ solution under controlled heating conditions. After the reaction, the residual permanganate was titrated, and COD_{Mn} was calculated from the amount of $KMnO_4$ consumed.

2.2.2 Satellite reflectance data

Surface reflectance data for model training was acquired for the 107 monitoring sites across the QTP and its surrounding areas from 2021 to 2023 using the Google Earth Engine (GEE) platform, based on Landsat-8 OLI/TIRS and Landsat-9 OLI-2/TIRS-2 imagery. For historical COD_{Mn} estimation in the source region of the Yellow River, surface reflectance data from Landsat-8/9 OLI/TIRS was also collected for 2014–2024 at 160 sites located at the headwater of the Yellow River (Fig. 1b). The Landsat-8/9 OLI datasets include five visible and near-infrared (VNIR) bands and two shortwave infrared (SWIR) bands. Atmospheric correction for Landsat-8/9 imagery was performed using the Land Surface Reflectance Code (LaSRC, v 1.5.0). Surface reflectance was extracted within a 90 m buffer around each site, and only pixels classified as water were retained. A minimum of 3×3 water pixels was required for a site–date matchup to be included. Pixels affected by clouds, cloud shadows, snow, ice, or non-water surfaces were removed based on the Landsat reflectance quality assessment bands.

2.2.3 Geographical feature data

Monthly precipitation and temperature data were obtained from the 1-km *Monthly Precipitation Dataset for China* (1901–2024) (Peng, 2025a, 2025b). Surface soil properties, including soil texture, pH, soil organic carbon, and bulk density, were extracted from the *Harmonized World Soil*

Database (Food and Agriculture Organization of the United Nations, 2021). Vegetation coverage data were sourced from the *China Regional 250-m Fractional Vegetation Cover Dataset* (2000–2024) (Gao et al., 2025). Land use data were derived from the *Land Use Dataset of China* (1980–2015) provided by the Resource and Environmental Science Data Center, Chinese Academy of Sciences (2020). Human Activity Intensity Index (HAII) were obtained from the *Human Activity Intensity Dataset of the Qinghai–Tibet Plateau* (2000–2020) (Liu, 2023). The Human Activity Intensity Index was calculated based on key human activity data, including agricultural and animal husbandry practices, industrial and mining development, urbanization, tourism, major ecological engineering projects, and pollutant discharge. Digital Elevation Model (DEM) data were retrieved from https://viewfinderpanoramas.org. Historical discharge data at C1, M1, M2 and M4 were compiled from multiple published sources (Wang, 2024; Liu et al., 2025), which are based on in-situ measurements from the same gauging network, and different sources were used to obtain complementary data. Future discharge projections were obtained from a single study and include the SSP126, SSP245, and SSP585 scenarios (M. Ma et al., 2023).

Future monthly temperature and precipitation data with spatial resolution of 1 km in the Yellow River source region were obtained from climate projections (Hu et al., 2025). This data was generated and bias corrected under three Shared Socioeconomic Pathways (SSPs) aligned with climate scenarios: SSP126 (sustainability-focused, low radiative forcing), SSP245 (intermediate, moderate stabilization), and SSP585 (fossil-fueled development, high radiative forcing).

2.3 Model development for historical COD_{Mn} reconstruction

2.3.1 Matching measured COD_{Mn} with satellite reflectance

180 COD_{Mn} data and satellite reflectance data (Landsat-8 OLI/TIRS and Landsat-9 OLI-2/TIRS-2)
181 acquired from 107 sites across the eastern QTP and adjacent regions during 2021–2023 were used
182 for model development (Fig. S2). Since Landsat-8/9 overpasses the study region at approximately
183 10:30 local time, COD_{Mn} measurements obtained at 08:00 or 12:00 on the same day were paired
184 with corresponding satellite scenes. When multiple valid matches were available, only the 12:00
185 COD_{Mn} measurement was retained to ensure temporal consistency. A total of 3048 valid COD_{Mn}–
186 reflectance matchups were obtained for the 107 sites during 2021–2023. These matched datasets
187 covered a broad COD_{Mn} concentration range (0.25–23.2 mg L^{-1}) and were used to develop models
188 for COD_{Mn} prediction.

189 **2.3.2 Input and prediction variables of models**

190 The 3048 valid COD_{Mn}–reflectance matchups were further processed to generate input variables.
191 Input features included raw spectral bands and derived indices, with COD_{Mn} serving as the
192 prediction variable. The raw spectral bands comprised Landsat-8/9 reflectance from Bands 1–7
193 and selected band ratios (SR_{nir}/SR_{red}, SR_{red}/SR_{green} and SR_{red}/SR_{blue}). Additionally, several spectral
194 indices known to be sensitive to organic matter were calculated (Table S1), namely the
195 Normalized Difference Chlorophyll Index (NDCI), Organic Carbon Index (OC_Index),
196 Normalized Suspended Material Index (NSMI), and Hue Angle (Yan et al., 2025). Longitude and
197 latitude were also incorporated as input variables.

198 **2.3.3 Model training**

199 AutoGluon is an open-source automated machine learning (AutoML) framework that builds
200 high-accuracy predictive models for tabular data through multi-layer model ensembling and
201 stacking. AutoGluon's *TabularPredictor* was configured in regression mode and trained using

multiple base learners (e.g., Gradient Boosting Machines, Random Forests, Neural Networks). The framework automatically optimized model selection, hyperparameters, and ensemble weights. Therefore, models for COD_{Mn} prediction were trained on Landsat-derived spectral features using AutoGluon-Tabular (v1.3.1) via its Python API in Python 3.8.3. The matched dataset (3048 pairs) described in Section 2.3.2 was randomly divided into training (80%) and testing (20%) subsets. A total training time limit of 600s was assigned to ensure sufficient exploration of model configurations.

2.3.4 Model evaluation

Model performance was evaluated using the negative Root Mean Squared Error (RMSE) for both the validation and test datasets (Eqs. 1–2). Lower (i.e., closer-to-zero) test and validation scores indicated superior model performance. The performance metrics for all models are summarized in Table S2.

$$RMSE = \sqrt{\frac{1}{n}\sum_{i=1}^{n}(y_i - \hat{y}_i)^2} \quad (1)$$

$$\text{Test /Validation score} = -RMSE \quad (2)$$

where, N denotes the size of the observations and y_i and $\hat{y}_i$ denote the in-situ values and satellite-retrieved values, respectively.

The importance of different input variables affecting the prediction of COD_{Mn} was also assessed based on the importance scores (Eq.3).

$$Importance\ (f_i) = M(D) - M(D_{_shuffled(f_i)}) \quad (3)$$

where, $M(\cdot)$, model performance metric (e.g., accuracy, log-loss, RMSE); D, original evaluation dataset; $D_{shuffled(fi)}$, same dataset, but with feature f_i randomly permuted; $Importance(fi)$, Drop in performance when f_i is destroyed.

2.3.5 Reconstruct of historical COD_{Mn}

The model exhibiting the highest test and validation scores was applied to reconstruct COD_{Mn} concentrations at 160 sites located in the headwater region of the Yellow River from 2014 to 2024 using Landsat-8 surface reflectance data. To evaluate model applicability and reliability, the reconstructed COD_{Mn} concentrations were compared with in situ measurements at two representative headwater sites. Two sites (M2 and M3) with abundant matched simulated and in-situ observations were selected to demonstrate the model's site-specific accuracy using the Mean Absolute Percentage Difference (MAPD), RMSE, and Bias, following the approach of Yan et al. (2025). Historical COD_{Mn} trends between 2014 and 2024 were assessed using the Mann–Kendall test and quantified using Sen's slope.

2.4 Prediction of future COD_{Mn} and its changes in the headstream of the Yellow River

To predict future COD_{Mn} levels at 160 sites in the headwaters of the Yellow River, the machine learning approach was also employed to model the relationships between geographical variables and the satellite-based estimates of COD_{Mn} levels. Soil texture (sand, silt, clay), bulk density, soil organic carbon, soil pH, altitude, human activity intensity, vegetation cover, land use, and ten-year averages of annual mean precipitation and temperature for each site during 2014-2024 were used as input features, while the ten-year average COD_{Mn} concentration for each site during 2014-2024 served as the target variable. The best-performing model, selected based on test and validation scores, was then used to predict future COD_{Mn} concentrations, incorporating both static variables (e.g., soil properties, vegetation cover, land use) and dynamic variables (future annual mean precipitation and temperature), depending on data availability. The projected future COD_{Mn} was model-based scenario projections conditional on the spatial stationarity assumption rather than

246 independently validated forecasts. Therefore, the selected model was used to learn the spatial
247 relationships between geographical/environmental characteristics and Landsat-derived COD_{Mn}
248 estimates, rather than directly learning an observed COD_{Mn} response. Satellite-based COD_{Mn}
249 estimates, rather than directly observed COD_{Mn} measurements were used in this model, prediction
250 uncertainty from the first-stage remote-sensing model can propagate into this model.

251 In order to predict the future COD_{Mn} using the trained model, future monthly temperature and
252 precipitation data was collected from Hu et al. (2025). The bias correction was performed by using
253 the delta Change Method (Text S1) to reconcile differences in temperature and precipitation data
254 sources (Beyer et al., 2020; Cao et al., 2026). Future annual mean precipitation and temperature
255 were then calculated for 2025-2040, 2041-2070, and 2071-2100, representing near-, mid-, and
256 long-term horizons. Future COD_{Mn} changes in the Yellow River source region for 2025-2040,
257 2041-2070, and 2071-2100 under SSP126, SSP245, and SSP585 scenarios were calculated relative
258 to the mean values from 2014–2024.

259 **2.5 Calculation of COD_{Mn} and DOC flux**

260 The COD_{Mn} flux in the source region of the Yellow River was calculated using Eq. 4:

261 $$F = C_i \times Q_i / 10 \quad (4)$$

262 where, F (Gg), nutrient export; C_i (mg/L), COD_{Mn} concentration at site i; Q_i (10^8 m³), river
263 discharge at site i. The DOC flux was calculated from the DOC–COD_{Mn} relationship in rivers
264 across China, expressed as $1.32F$ (Shang et al., 2026).

265 **3 Results**

266 **3.1 Performance of developed models**

267 **3.1.1 Predicting historical COD_{Mn} using Landsat reflectance data**

A total of 24 models were developed and evaluated to predict COD_{Mn} levels from Landsat reflectance data, with test and validation scores summarized in Table S2. The LightGBMLarge model demonstrated the highest predictive accuracy for COD_{Mn} across the QTP and surrounding regions, achieving test and validation scores of –0.22 and –0.67, respectively. Predicted versus in-situ measured COD_{Mn} levels for 2021–2023 based on training dataset are shown in Fig. 2a, with RMSE and R^2 of 0.33 and 0.93, respectively, indicating strong predictive performance.

The relative importance of input variables in the LightGBMLarge model was quantified using importance scores (Fig. 2b). The five most influential predictors were longitude, latitude, SR_{Red}/SR_{Green}, NSMI, and Band 1. Based on its performance, the LightGBMLarge model was selected to estimate historical COD_{Mn} levels in the source region of the Yellow River.

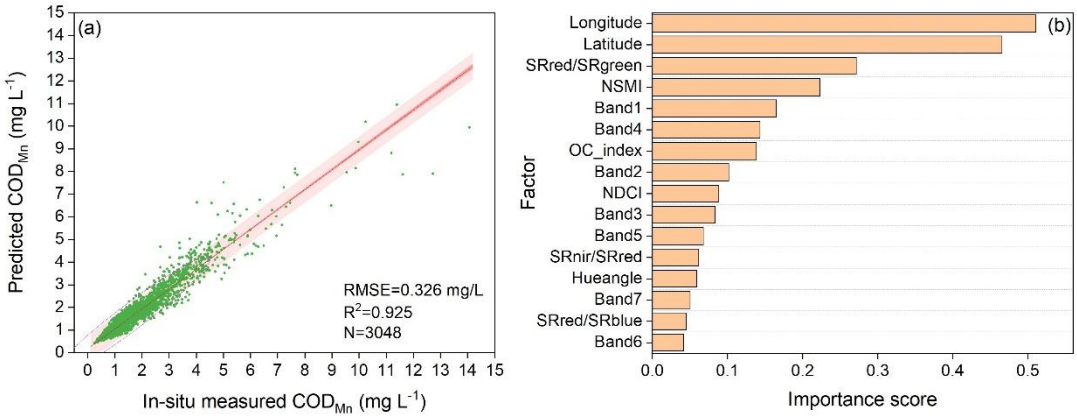


Fig.2 Model performance for COD_{Mn} prediction based on training set using Landsat 8/9 reflectance data (a), and importance of input variables in COD_{Mn} prediction (b).

To present a clearer site-level model reliability, two representative sites (M2 and M3) in the Yellow River headwaters were used to compare modeled and in-situ COD_{Mn} time series (Fig. 3). The results indicate that the model can accurately capture both spatial and temporal variability of riverine COD_{Mn} in the headstreams of the Yellow River. At site M3, RMSE, MAPD, and Bias

were 0.12 mg L^{-1}, 8.16%, and –2.38%, respectively, and RMSE, MAPD, and Bias at site M2 were 0.58 mg L^{-1}, 15.32%, and –2.23%, respectively.

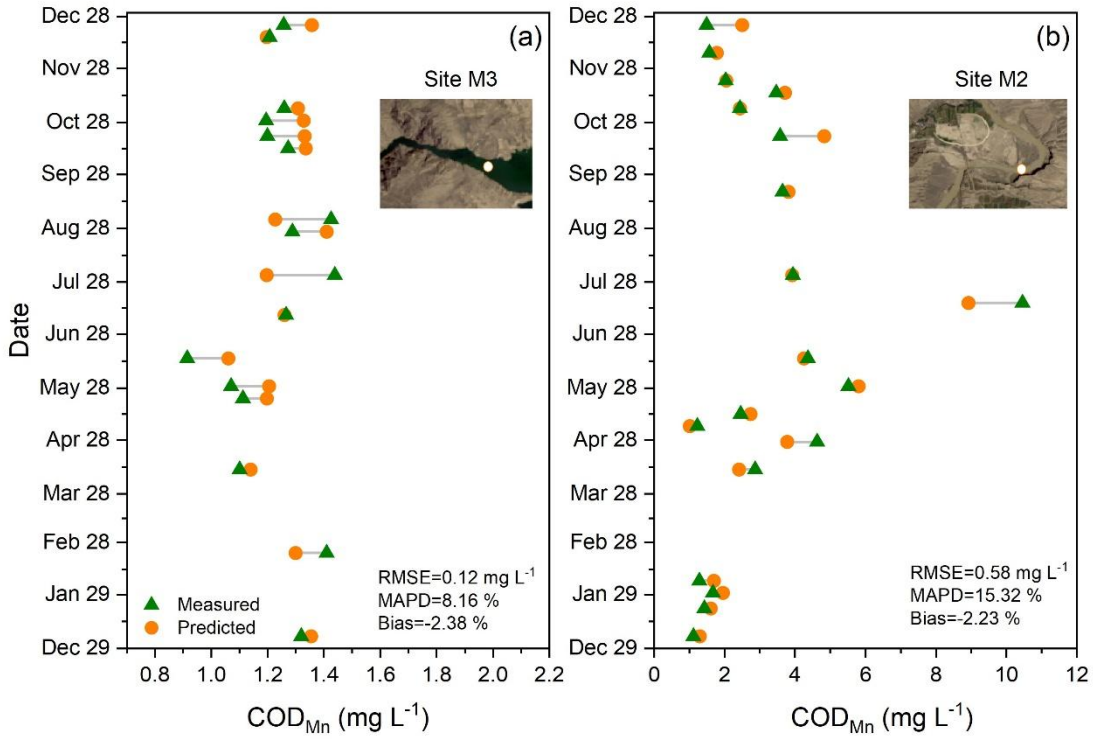


Fig.3 Comparison between predicted and measured COD_{Mn} values in 2023 at sites M3 (a) and M2 (b) within the Yellow River source region.

3.1.2 Prediction of future COD_{Mn} using geographical features

A total of 36 models for predicting future COD_{Mn} based on geographical features were evaluated (Table S3), and the LightGBMLarge model exhibited the highest performance, with test and validation scores of –0.08 and –0.26, respectively. Predicted versus satellite-based estimates of average COD_{Mn} levels based on the training dataset in the Yellow River source region are presented in Fig. 4a, achieving an R^2 of 0.91 and an RMSE of 0.18, indicating strong predictive capability of this model. Analysis of feature importance revealed that altitude, precipitation, temperature, and vegetation contributed most significantly to COD_{Mn} variability in the study area

(Fig. 4b).

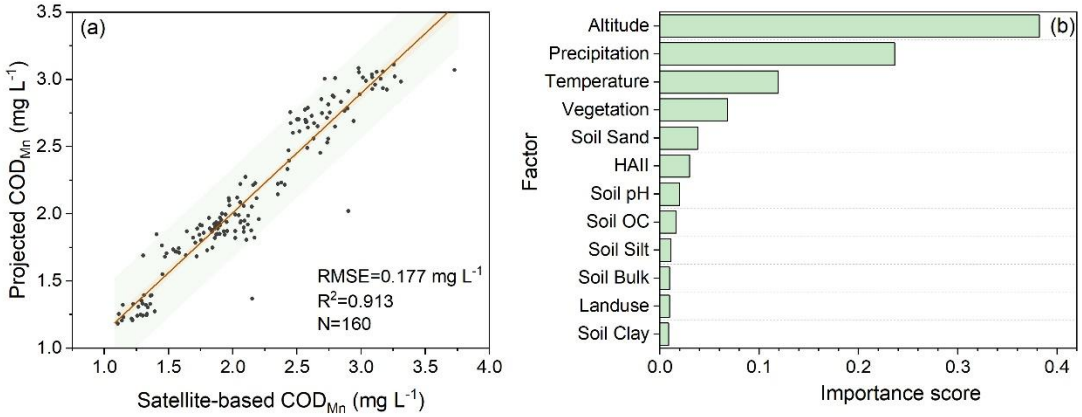


Fig.4 Performance of the developed model for COD_{Mn} prediction based on the training set using geographical feature data (a), and importance of variables in the predictive model (b). HAII is Human Activity Intensity Index; Soil OC represents soil organic carbon; Soil Bulk is soil bulk density; Soil Sand, Clay and Silt are soil texture.

3.2 Spatiotemporal changes of COD_{Mn} in the headstream of the Yellow River

The developed model estimated an annual mean COD_{Mn} concentration of 2.14 ± 1.06 mg L^{-1} in the Yellow River source region from 2014 to 2024, with pronounced spatial variability. In the upstream area, the mean COD_{Mn} was 1.89 ± 0.81 mg L^{-1}, while higher concentrations were observed in the mid-downstream region (2.73 ± 1.63 mg L^{-1}). The downstream area, which includes large reservoirs such as Longyangxia and Lijiaxia, exhibited significantly lower COD_{Mn} levels (1.54 ± 0.50 mg L^{-1}) (Fig. 5a, b).

Over the past decade, the midstream region showed a clear increasing trend in COD_{Mn}, with an average rise of 0.58 mg L^{-1} (Fig. 5c, d). In contrast, the upstream area exhibited both increasing and decreasing trends, with a mean change of 0.08 mg L^{-1}, whereas COD_{Mn} concentrations in the downstream region remained relatively stable (mean change: –0.10 mg L^{-1}). However, the

historical COD_{Mn} trend was not statistically significant in the headwater region of the Yellow River (Fig. S3).

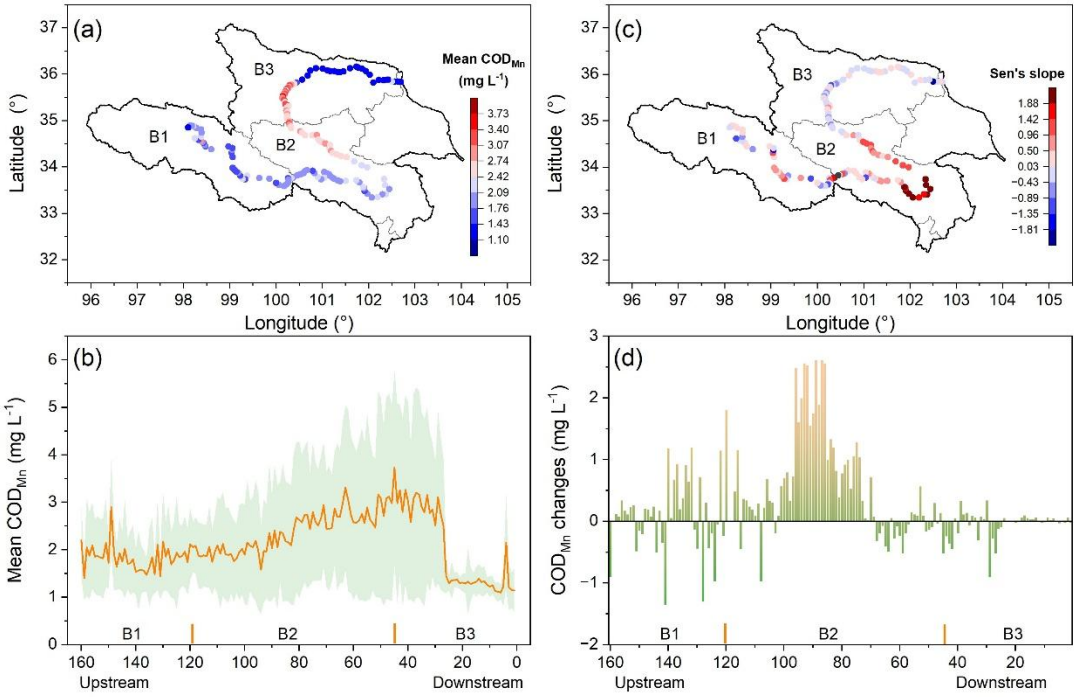


Fig.5 Spatial variation of mean COD_{Mn} (a, b), Sen's slope per decade for historic COD_{Mn} trend (c), and COD_{Mn} changes during 2014–2024 (d) in the Yellow River source region. Historic COD_{Mn} trend during 2014-2024 was assessed using the Mann–Kendall test and quantified using Sen's slope (mg COD_{Mn} L^{-1} $decade^{-1}$).

Seasonal variations of COD_{Mn} were also evident during our study. Average monthly COD_{Mn} concentrations ranged from 0.8 to 8.0 mg L^{-1} (Fig. 6). The downstream site maintained low (0.8-2.4 mg L^{-1}) and showed higher COD_{Mn} levels in summer (Fig. 6a), while the midstream site exhibited a pronounced increase from March, peaking in July (~8 mg L^{-1}), followed by a gradual decline (Fig. 6b). The upper–midstream site displayed two distinct peaks in late spring and summer, suggesting episodic organic inputs associated with ice melt and rainfall (Fig. 6c).

Upstream sites remained low to moderate (1-3 mg L^{-1}) with minimal seasonal variation (Fig. 6d).

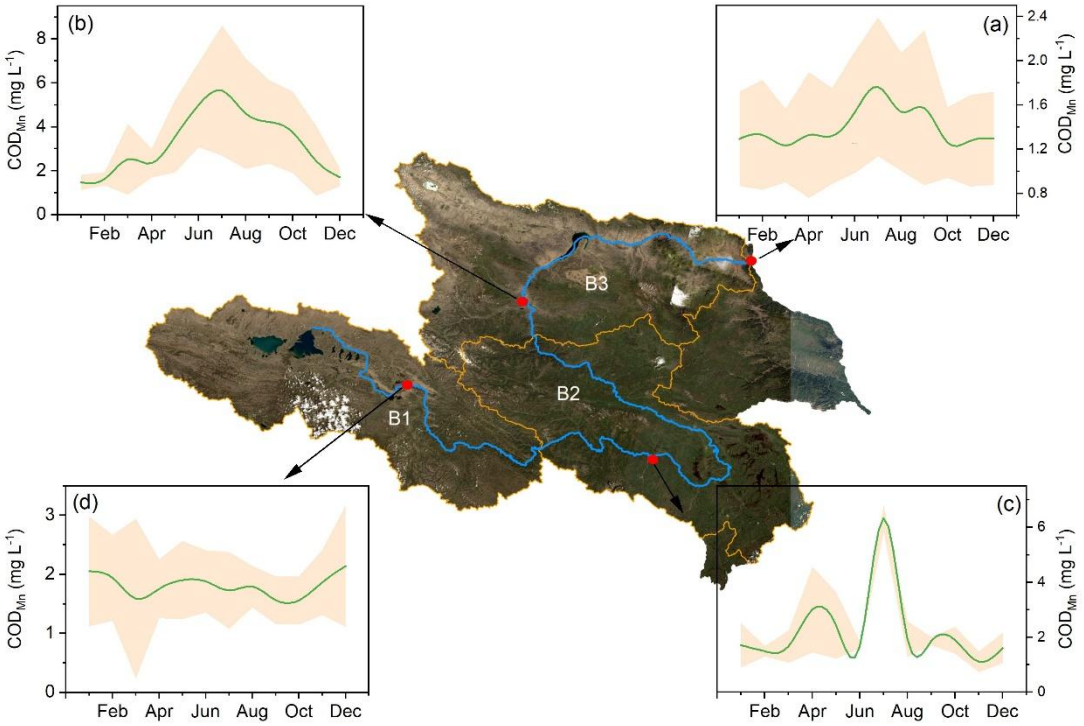


Fig.6 Averaged monthly variations of COD_{Mn} during 2014–2024 within the Yellow River source region.

3.3 Future climate and COD_{Mn} changes in the source region of the Yellow River

Across all scenarios and periods, precipitation exhibits a consistent spatial pattern, increasing from upstream reaches to a midstream maximum and subsequently decreasing toward downstream sections (Fig. 7a-c). This pattern is preserved under all SSPs, although the magnitude of precipitation varied among scenarios and time slices. Relative to current conditions, precipitation increases slightly in the midstream region under SSP126 and SSP245, particularly during the mid- and late-century periods. Under SSP585, precipitation displays enhanced increase, with higher midstream values during 2041–2070 and 2071–2100 and lower precipitation toward downstream reaches.

Compared with current conditions, future temperature rises across the entire study area (Fig. 7d-f), with the magnitude of warming increasing over time and from SSP126 to SSP585. Under SSP126, temperature increases are relatively moderate, whereas SSP245 shows stronger warming, especially during 2071–2100. The largest temperature increases occurred under SSP585, with pronounced downstream variability during the late-century period, resulting in an amplified longitudinal temperature gradient.

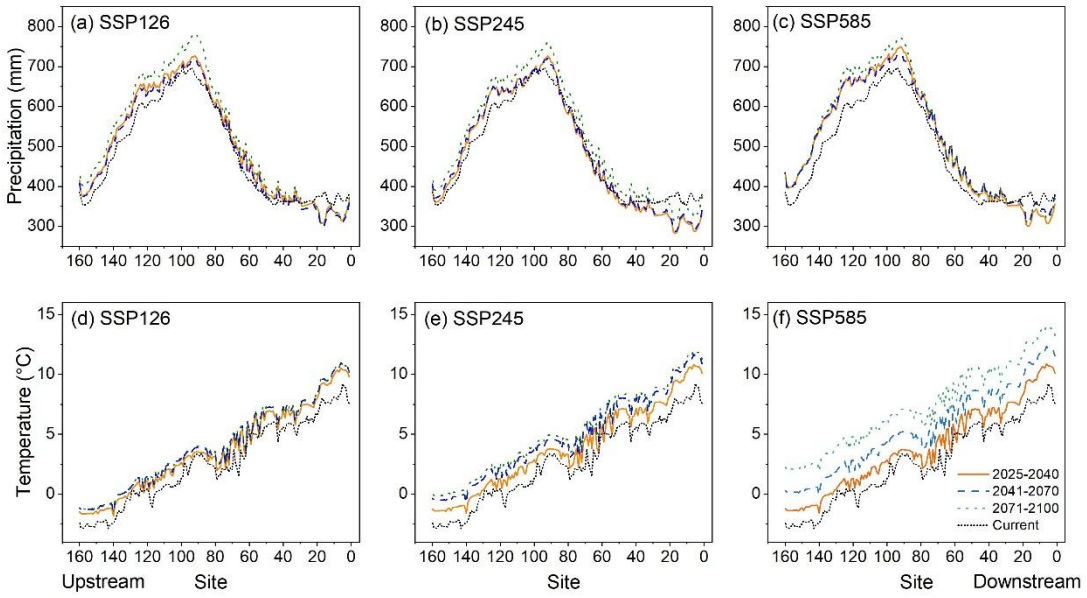


Fig.7 Projected precipitation and temperature variations for 2025-2040, 2041-2070, and 2071-2100 under SSP126, SSP245, and SSP585 scenarios.

Projected changes in COD_{Mn} across the study area show pronounced spatial and temporal variability under all three scenarios (Fig. 8). During the near-term period (2025–2040), COD_{Mn} changes are generally modest, with most monitoring sites exhibiting values close to zero. In the mid-term period (2041–2070), the COD_{Mn} changes show an overall increase, with mean value of 0.05 mg L^{-1}. Specifically, midstream sites more frequently experience decreases in COD_{Mn},

whereas upstream and downstream regions display a mixture of small increases and decreases. By the late-century period (2071–2100), the average change in COD_{Mn} is -0.01 mg L^{-1}. COD_{Mn} shows a pronounced decrease trend in the midstream area (-0.12 mg L^{-1}) under SSP585. Upstream and downstream areas show a higher occurrence of positive COD_{Mn} changes. Overall, COD_{Mn} shows a slight increasing trend across the three scenarios over different periods, with 877 positive changes (61%) and 563 negative changes (39%).

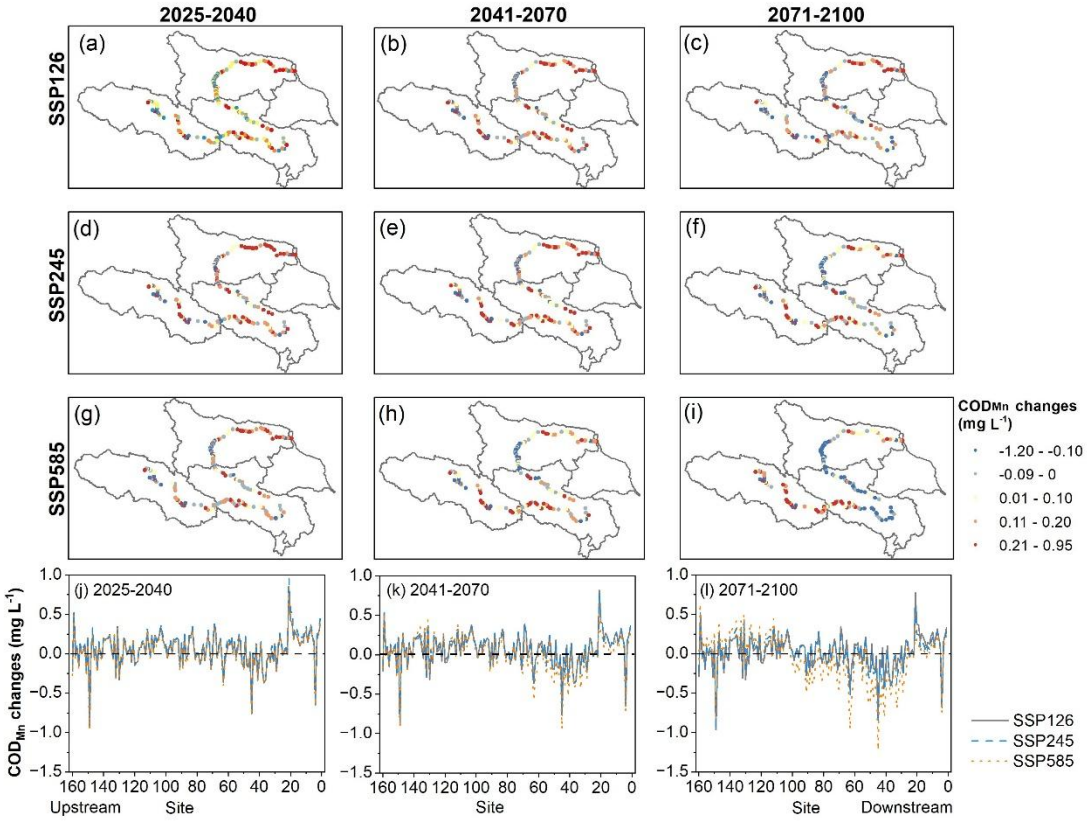


Fig.8 Projected spatial variation of COD_{Mn} changes in the Yellow River source region for 2025-2040, 2041-2070, and 2071-2100 under SSP126, SSP245, and SSP585 scenarios. COD_{Mn} changes were calculated relative to the mean values from 2014–2024.

3.4 Historical and future riverine organic matter exports

Historical and future COD_{Mn} and converted DOC exports are shown in Fig. 9 and Fig. S4,

374 respectively. Based on the annual average discharge at control site M4 (1987–2021),
375 approximately 28.1 Gg of COD_{Mn} (37.1 Gg DOC) was exported from the entire study area. In
376 contrast, the annual mean COD_{Mn} export at site M2 was 62.5 Gg (82.5 Gg DOC), indicating that
377 approximately 34 Gg of COD (44.8 Gg DOC) was either deposited or decomposed between M4
378 and M2 along the downstream of the Yellow River's source region. The export of riverine organic
379 matter primarily occurred during the wet season (June–October) (Figs. 9a, S4a), which contributes
380 substantially to the annual dissolved organic matter export from the source region (Figs. 9b, S4b).
381 Additionally, the observed increase in COD_{Mn} or DOC export between sites M1 and M2 highlights
382 the midstream region as a major source of dissolved organic matter (Figs. 9b, S4b).
383 Though the projected discharge presents an overall increase trend (Fig. 9c), the calculated
384 future COD_{Mn} (or DOC) export at site M2 indicates a slight declining trend under the three
385 scenarios (Figs. 9d, S4c). For example, the average COD_{Mn} export at M2 under different scenarios
386 is expected to decrease from 62.5 Gg to 59.6 Gg (82.5 Gg to 78.7 Gg DOC) by 2100.

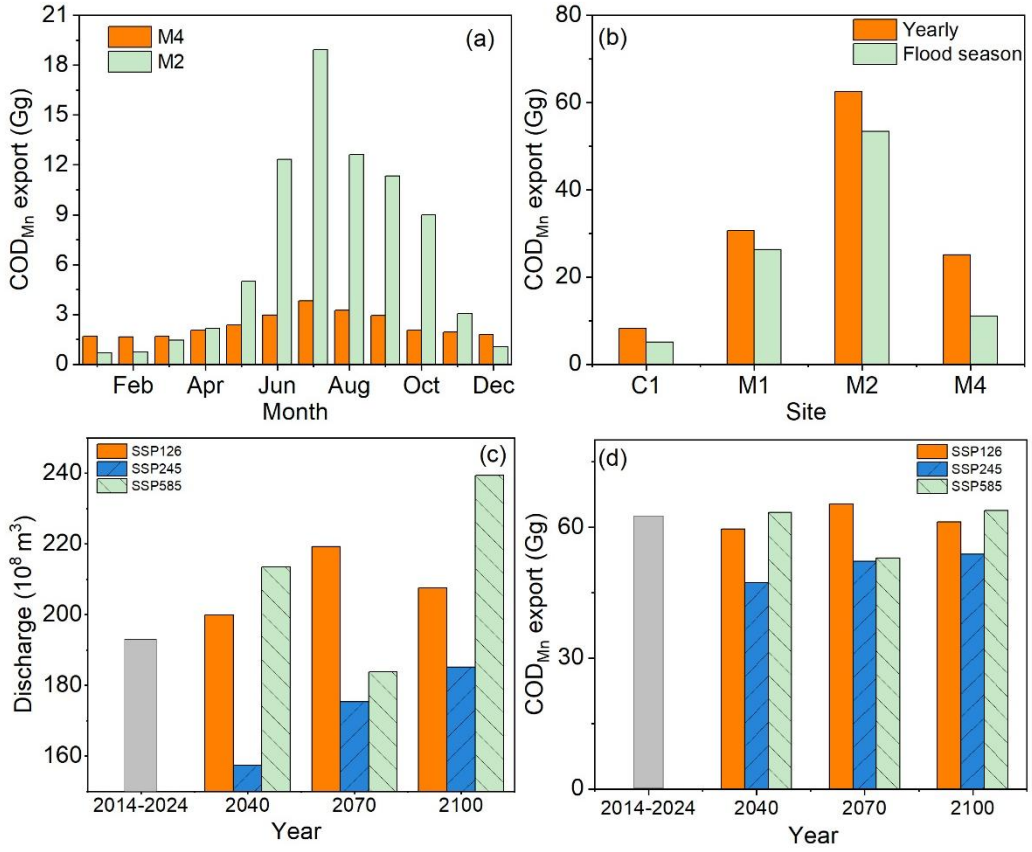


Fig.9 Monthly average COD_{Mn} export at sites M2 and M4 during 2014-2024 (a); comparison between annual and flood-season COD_{Mn} exports (b); projected annual average discharge collected from M. Ma et al. (2023) (c), and projected COD_{Mn} export at M2 for 2040, 2070, and 2100 under SSP126, SSP245, and SSP585 scenarios (d).

4 Discussion

4.1 Factors driving riverine organic matter dynamics in the headstream of the Yellow River

4.1.1 Spatial variations

Primary sources of riverine organic carbon include losses from soils, plant litter, root exudates in grasslands, and permafrost thaw via surface runoff (Yan et al., 2023). In this study, precipitation, temperature, vegetation, and soil texture were identified as key drivers of COD_{Mn} variation (Fig. 4b). Notably, the overall soil organic carbon, vegetation cover, fine particle content, and

precipitation are higher in the midstream region of the headwater (Fig. S5), providing abundant carbon sources and facilitating transport to nearby rivers, resulting in elevated COD_{Mn} levels and fluxes in the mid-downstream areas (Figs. 5a, 9a, b). Additionally, bare land in the mid-downstream areas of the headstream may also contribute to the soil erosion and the associated organic carbon losses (Fig. S1). L. Li (2025) identified the higher lateral fluxes of river organic matter in the midstream area of the Yellow River' s source region. Consequently, the midstream area represents a critical source of organic carbon for the Yellow River headwaters.

In contrast, COD_{Mn} levels decreased markedly in the downstream region (Figs. 5a, b). This decline is likely driven by damming, as three large reservoirs, Longyangxia, Laxiwa, and Lijiaxia have been constructed in the downstream headwater region since the 1970s. Reservoirs increase water residence time, promoting deposition and decomposition of organic carbon, greenhouse gas emissions, and uptake by aquatic plants (Maavara et al., 2017, 2020). Therefore, the deposition or decomposition of organic matter along the downstream areas may contribute to the decline of COD_{Mn} levels. The deposition of riverine organic matter can be inferred from the decrease in COD_{Mn} (or DOC) fluxes at the outlet (M4) of the study area relative to site M2 (Figs. 9, S4). L. Li et al. (2025) also reported negative dissolved organic matter fluxes in the main channels of the Yellow River's headstreams. Additionally, the decomposition of the deposited organic matter is evidenced by CO_2 outgassing from the river water. Previous study has found that CO_2 outgassing from the cascade reservoirs of Yellow River's source region was estimated at 131 ± 156 mmol m^{-2} d^{-1} in dry seasons and 466 ± 366 mmol m^{-2} d^{-1} in flood seasons (Wang et al., 2022). Therefore, these observations suggest that the sedimentation and degradation of organic matter contributes to lower COD_{Mn} concentrations in the downstream area.

The COD_{Mn} concentration remained relatively stable along the upper to middle reaches of the Yellow River's headwaters. This region is characterized by permafrost and seasonally frozen ground, with low precipitation and limited runoff (Yang et al., 2023). Surface runoff in this area primarily originates from precipitation, snowmelt, and glacier melt (Li et al., 2025). Consequently, due to the relatively uniform and stable runoff and land cover, COD_{Mn} levels exhibited a homogeneous spatial distribution along the upper to middle reaches of the Yellow River's headwaters.

4.1.2 Temporal variations

Climate-driven changes in runoff and temperature strongly influence catchment-scale carbon dynamics, altering riverine organic matter fluxes globally (Costa et al., 2023). Over the past decade, air temperature in the source region of the Yellow River has shown an increasing trend, with a basin–averaged increase of 0.67 °C, and the precipitation also presented an over increase trend though decrease slightly after 2019 (Fig. S6). The study area is particularly sensitive to warming-induced permafrost thaw, glacier melting, soil erosion, and intensified human activities over recent decades (Chen et al., 2022; Deng et al., 2025; Lan et al., 2025), which modify organic matter sources and lateral transport between terrestrial and aquatic systems, affecting ROM levels and fluxes in rivers (Wang et al., 2020; Chen et al., 2022; S. Wang et al., 2025). For example, previous studies highlighted that permafrost thaw was projected to release 129 ± 21.02 Tg soil organic carbon annually (Lan et al., 2025). Glacier melting contributes an estimated 0.19 Tg C yr^{-1} as dissolved organic carbon (Chen et al., 2022). Intensified rainfall has increased soil erosion by 42% over the past four decades, resulting in an average soil carbon loss of 4 ± 1.2 Tg C yr^{-1} (Deng et al., 2025).

Therefore, affected by the increased temperature and precipitation, COD_{Mn} concentrations in the source region of the Yellow River exhibited an overall increasing trend over the past decade, with an average rise of 0.26 mg L^{-1} (Fig. 5c, d). Especially the midstream region experienced the most pronounced increase (0.58 mg L^{-1}). The higher precipitation combined with increased runoff likely enhance organic matter leaching from grasslands, contributing to the rise of riverine COD_{Mn} in the midstream area (Yang et al., 2023; Chen et al., 2025).

In addition to climate effects, growing human activities such as land use changes, grazing, and construction on the QTP also influence carbon mobilization (Chen et al., 2022). Human-induced land-use changes, grassland degradation, construction activities, and overgrazing can lead to organic matter losses in the study area. In addition, the construction and urbanization of natural and agricultural ecosystems may further accelerate organic matter losses within the watershed. All these human activities may contribute to the rising of COD_{Mn} in the headstream of the Yellow River.

4.2 Future riverine organic matter changes in the headstream of the Yellow River under climate change

Rapid climate change in alpine regions is altering carbon cycling in both terrestrial and aquatic ecosystems (Chen et al., 2022). As carbon dynamics are highly sensitive to climatic variations, warming and wetting trends are expected to influence the stability of riverine organic matter in alpine catchments. Numerous studies indicate that precipitation and temperature on the QTP are projected to increase throughout this century, particularly in high-elevation areas (Meng et al., 2023; Karim et al., 2025). Our projections also suggest an overall increase in precipitation, especially in the up-midstream area of the Yellow River source region (Fig. 7), and significant

466 warming is projected in the whole study area by 2100, especially under SSP245 and SSP585.
467 Climate-driven changes are expected to induce the largest variability in COD_{Mn} concentrations in
468 the midstream region (Fig. 8). COD_{Mn} levels are projected to increase in most parts of the source
469 region of the Yellow River, whereas annual average COD_{Mn} exports from the whole catchment
470 will decrease slightly from 62.5 Gg to 59.6 Gg (82.5 Gg to 78.7 Gg DOC) (Figs. 9d, S4c).

471 ROM dynamics are jointly regulated by organic matter supply and hydrological processes
472 within catchments (Li et al., 2022; Wu et al., 2024). Increased precipitation can enhance surface
473 runoff, leading to losses of organic matter from the catchment, and COD_{Mn} concentrations may be
474 diluted as discharge continues to increase. The projected warming in the headwater area of the
475 Yellow River will lead to the continuing permafrost degradation, promoting the loss of organic
476 matter within the catchment and leading to the increase of the COD_{Mn} level in the headstreams. In
477 addition, damming prolongs water residence time, promoting organic matter deposition in cascade
478 reservoirs in the downstream area of the Yellow River's source region and reducing the riverine
479 organic matter export from the study area. Under warm conditions, the degradation of deposited
480 organic matter in the bottom of the reservoir may be enhanced, releasing additional organic carbon
481 from reservoir sediments and contributing to the rise of COD_{Mn} levels in the downstream area
482 (Vachon et al., 2021; Battin et al., 2023).

483 However, the extent to which organic matter reaches rivers depends on hydrological
484 processes and connectivity between the source region and river channels. The characteristics of
485 rainfall events may shift the ROM response to storms from transport-limited to supply-limited,
486 thereby reducing ROM levels (Li et al., 2022). Consequently, the projected increase in
487 precipitation by the 2100s is expected to lead to a decrease in COD_{Mn} levels within the midstream

areas (Fig. 8). In addition, permafrost thaw induced by the warming can also alter runoff pathways, promoting subsurface flow and potentially reducing surface discharge to rivers (Yang et al., 2023). Increased vegetation cover can also reduce transport of organic matter through reducing soil erosion and surface runoff (W. Ma et al., 2023; Liu et al., 2024). Therefore, the export of DOC from the headwaters of the Yellow River may remain stable or decrease slightly under the combined effects of climate change, hydrological variability, permafrost degradation, and human activities.

4.3 Uncertainty in riverine organic matter dynamics on the QTP

Understanding riverine organic matter dynamics is essential for assessing aquatic ecosystem feedback to climate change. Ongoing warming and wetting on the QTP are expected to alter carbon stability, increasing uncertainty in watershed organic matter losses (Bai et al., 2025). For instance, increased precipitation may enhance surface runoff, however, rising temperatures can also decrease catchment runoff by enhancing evaporation. The influence of hydrological processes on ROM dynamics depends on the characteristics of the catchment (Li et al., 2022). Previous studies have predicted both increasing and decreasing streamflow trends on the QTP under future climate scenarios (Yang et al., 2023; Li et al., 2025; San et al., 2025). Increased streamflow may elevate COD_{Mn} in rivers, or dilute COD_{Mn} due to higher streamflow. Conversely, reduced streamflow may decrease organic matter transport to rivers or concentrate COD_{Mn} in river water.

Additionally, warming-induced permafrost thaw may accelerate topsoil organic matter mobilization, stimulate microbial activity, and promote soil organic matter decomposition, releasing more dissolved organic matter (Ziliang Li et al., 2025). However, the frozen ground degradation can also result in the decreased surface runoff by increasing the subsurface runoff

(Yang et al., 2023). Vegetation greening on the QTP may both enhance soil carbon storage and reduce organic matter losses to river networks through mitigating soil erosion (Deng et al., 2025). Therefore, climate change can further differentially affect terrestrial carbon stocks and carbon losses, introducing additional complexity and uncertainty in catchment-scale organic matter sources and transport (Chen et al., 2022; W. Ma et al., 2023; Liu et al., 2024).

In-stream carbon biogeochemical processes are also highly complex under changing climatic conditions. Organic matter decomposition depends on temperature, redox conditions, hydrology, microbial activity, and organic matter characteristics (Battin et al., 2023). The climate change is projected to change the hydrological processes and the associated biogeochemical processes, further altering the carbon cycling in the alpine rivers. However, interactions among these factors are not fully understood in alpine rivers, making predictions of alpine river metabolism and carbon budget under climate change uncertain (Li et al., 2025).

Anthropogenic activities on the QTP further contribute to uncertainty. Warming and wetting may expand farming, increasing soil erosion and carbon losses (Chen et al., 2022). Future dam construction alters organic matter transport by promoting deposition, influencing greenhouse gas emissions, and facilitating organic matter degradation (Battin et al., 2023). Conversely, ecological restoration, such as afforestation, can increase soil organic matter accumulation and litterfall (Chen et al., 2022; Yan et al., 2023), leading to increase in organic matter and the COD_{Mn} levels in the alpine Rivers.

4.4 Limitations of this study

In this study, we project a general increase in levels and fluxes of COD_{Mn} based on modeled temperature, precipitation, and discharge. However, future climatic trends may deviate from

current projections, and the predicted temperature and precipitation may not represent the actual future patterns. Besides, our developed model does not incorporate changes in land covers, soil carbon stocks, hydrological processes, or in-stream carbon biogeochemistry, all of which may significantly influence riverine carbon cycling. Therefore, future research should integrate these factors to develop more precise, process-based models and improve understanding of carbon dynamics in alpine river catchments.

In addition, future COD_{Mn} projection model is trained on COD_{Mn} values predicted by the first-stage retrieval model rather than on independent long-term observations, so the two models are not statistically independent and retrieval errors inevitably propagate into the climate projections. The extrapolating spatial "geographical characteristics—COD_{Mn} concentration" relationships to temporal climate change represents a space-for-time substitution that assumes stationarity, an assumption that is difficult to test rigorously with the available data. Finally, COD_{Mn} is an oxygen-equivalent index rather than a direct measure of organic matter or carbon. The DOC export estimated in this study was derived from a simplified empirical relationship between COD_{Mn} and DOC in rivers across China, which may introduce additional uncertainty into the DOC estimates.

5 Conclusions

In this study, LightGBM-Large models were developed to reconstruct the historical variations of COD_{Mn} in the source region of the Yellow River and to predict its future changes. Our findings identify the midstream region of the Yellow River's headstream, with higher COD_{Mn} levels (2.73 ± 1.63 mg L^{-1}), is sensitive to climate change and exhibited an increasing trend of COD_{Mn} (0.58 mg L^{-1}) in the past decade. Precipitation and temperature were identified as the key factors

554 influencing COD_{Mn} dynamics in the headwaters of the Yellow River. Future projections suggest
555 that increased precipitation and temperature may lead to an overall rise of COD_{Mn} levels, with
556 decrease in some specific sites. The export of dissolved organic matter from the headwaters of the
557 Yellow River is projected to remain stable or decrease slightly in the future. However, the limited
558 spatial and temporal resolution of Landsat data and lack of geophysical data, still poses challenges
559 for accurately capturing rapid variations in riverine organic matter in the source region of the
560 Yellow River. Therefore, future research in alpine rivers should focus on developing more robust
561 models by integrating long-term and high-resolution satellite observations and in-situ observations
562 and incorporating a broader range of environmental variables.

563 **Data availability**

564 Water quality data in this study are obtained from the China National Environmental Monitoring
565 Centre (https://www.cnemc.cn). Historical monthly precipitation and temperature, surface soil
566 properties, vegetation coverage, and projected future monthly temperature and precipitation data
567 are obtained from the Tibetan Plateau Data Centre (https://data.tpdc.ac.cn). The modeled historical
568 and projected future COD_{Mn} data in this study are openly available on Zenodo
569 (https://doi.org/10.5281/zenodo.22766232).

570 **Author contributions**

571 **XW**: Conceptualization, Methodology, Writing original draft, Funding acquisition; **JW**:
572 Methodology, Data curation, Review and editing; **TR**: Investigation, Formal analysis, Validation;
573 **JZ**: Validation, Conceptualization, Review and editing.

574 **Competing interests**

575 The authors declare that they have no conflict of interest.

Acknowledgments

We thank the National Tibetan Plateau/Third Pole Environment Data Center (TPDC) for providing the environmental data, and Google Earth Engine (GEE) for the river surface reflectance data used in this study. We also thank the editors and the two anonymous reviewers for their careful reading, insightful comments, and constructive suggestions, which have greatly helped us improve this manuscript.

Financial support

This study was funded by China West Normal University (22kA001), the Sichuan Science and Technology Program (2026YFTX0001), and the Natural Science Foundation of Sichuan Province (2026NSFSC0226).

References

Adegun, A., Viriri, S., Tapamo, J.-R., 2023. Review of deep learning methods for remote sensing satellite images classification: experimental survey and comparative analysis. Journal of Big Data 10. https://doi.org/10.1186/s40537-023-00772-x

Aryal, S., Pokhrel, Y., 2025. Spatio-temporal heterogeneities in hydrologic dynamics across the Asian Water Tower. Journal of Hydrology 662, 133951. https://doi.org/10.1016/j.jhydrol.2025.133951

Bai, Y., Peng, Y., Zhang, D., Yang, G., Chen, L., Kang, L., Zhou, W., Wei, B., Xie, Y., Yang, Y., 2025. Heating up the roof of the world: tracing the impacts of in-situ warming on carbon cycle in alpine grasslands on the Tibetan Plateau. National Science Review 12, nwae371. https://doi.org/https://doi.org/10.1093/nsr/nwae371

Battin, T.J., Lauerwald, R., Bernhardt, E.S., Bertuzzo, E., Gener, L.G., Hall, R.O., Hotchkiss, E.R.,

598 Maavara, T., Pavelsky, T.M., Ran, L., Raymond, P., Rosentreter, J.A., Regnier, P., 2023. River
599 ecosystem metabolism and carbon biogeochemistry in a changing world. Nature 613, 449–
600 459. https://doi.org/10.1038/s41586-022-05500-8
601 Beusen, A.H.W., Doelman, J.C., Van Beek, L.P.H., Van Puijenbroek, P.J.T.M., Mogollón, J.M.,
602 Van Grinsven, H.J.M., Stehfest, E., Van Vuuren, D.P., Bouwman, A.F., 2022. Exploring river
603 nitrogen and phosphorus loading and export to global coastal waters in the Shared
604 Socio-economic pathways. Global Environmental Change 72, 102426.
605 https://doi.org/10.1016/j.gloenvcha.2021.102426
606 Beyer, R., Krapp, M., Manica, A., 2020. An empirical evaluation of bias correction methods for
607 palaeoclimate simulations. Clim. Past 16, 1493–1508.
608 https://doi.org/10.5194/cp-16-1493-2020
609 Cao, Y., Yao, H., Zhang, C., Gu, C., Yang, L., Hao, R., Li, X., Wang, Z., Xiao, H., Wang, J., Shi, Z.,
610 2026. Data-driven assessment of nitrogen and phosphorus buffering capacity across 460
611 Chinese watersheds: Spatial patterns, drivers, and future projections. Water Research 293,
612 125424. https://doi.org/10.1016/j.watres.2026.125424
613 Chen, H., Ju, P., Zhu, Q., Xu, X., Wu, N., Gao, Y., Feng, X., Tian, J., Niu, S., Zhang, Y., 2022.
614 Carbon and nitrogen cycling on the Qinghai–Tibetan Plateau. Nature Reviews Earth &
615 Environment 3, 701–716. https://doi.org/10.1038/s43017-022-00344-2
616 Chen, Y., Xu, C., Liu, Wenjun, De Boeck, H.J., Zhou, H., Chen, Q., Ma, Y., Liu, Weihong, Zhao,
617 L., Wang, H., Chen, J., Zhang, Y., Zhang, Z., 2025. Machine learning-based assessment of
618 grassland degradation levels on the Qinghai-Tibet Plateau from 2000 to 2020. Ecological
619 Indicators 180, 114360. https://doi.org/10.1016/j.ecolind.2025.114360

620 Costa, D., Sutter, C., Shepherd, A., Jarvie, H., Wilson, H., Elliott, J., Liu, J., Macrae, M., 2023.
621 Impact of climate change on catchment nutrient dynamics: insights from around the world.
622 Environ. Rev. 31, 4–25. https://doi.org/10.1139/er-2021-0109
623 Deng, R., Li, D., Zhao, Y., Walling, D.E., Panagos, P., Borrelli, P., Ciais, P., Huang, Y., Bai, Y.,
624 Chalov, S., Golosov, V.N., Fu, X., Miao, C., Wei, J., Ni, J., 2025. Intensified rainfall overrides
625 vegetation greening in driving erosion and carbon loss on the Tibetan Plateau. Science
626 Bulletin. https://doi.org/10.1016/j.scib.2025.09.005
627 Deng, Y., Zhang, Y., Pan, D., Yang, S.X., Gharabaghi, B., 2024. Review of Recent Advances in
628 Remote Sensing and Machine Learning Methods for Lake Water Quality Management.
629 Remote Sensing 16. https://doi.org/10.3390/rs16224196
630 Food and Agriculture Organization of the United Nations, I.I. for A.S.A., 2021. China soil map
631 based harmonized world soil database (HWSD) (v1.1) (2009). National Tibetan Plateau Data
632 Center.
633 Gao, J., Shi, Y., Zhang, H., Chen, X., Zhang, W., Shen, W., Xiao, T., Zhang, Y., 2025. China
634 regional 250m fractional vegetation cover data set (2000-2024). National Tibetan Plateau
635 Data Center. https://doi.org/10.11888/Terre.tpdc.300330
636 Giri, S., 2021. Water quality prospective in Twenty First Century: Status of water quality in major
637 river basins, contemporary strategies and impediments: A review. Environmental Pollution
638 271, 116332. https://doi.org/10.1016/j.envpol.2020.116332
639 Hong, J., Pang, B., Zhao, L., Shu, S., Feng, P., Liu, F., Du, Z., Wang, X., 2025. Soil phosphorus
640 crisis in the Tibetan alpine permafrost region. Nat Commun 16.
641 https://doi.org/10.1038/s41467-025-61501-x

642 Hu, M., Liu, Y., Zhang, Y., Shen, H., Yao, M., Dahlgren, R.A., Chen, D., 2020. Long-term (1980–
643 2015) changes in net anthropogenic phosphorus inputs and riverine phosphorus export in the
644 Yangtze River basin. Water Research 177, 115779.
645 https://doi.org/10.1016/j.watres.2020.115779
646 Hu, X., Shi, S., Zhou, B., Ni, J., 2025. A 1 km monthly dataset of historical and future climate
647 changes over China. Sci Data 12, 436. https://doi.org/10.1038/s41597-025-04761-y
648 Jiao, N., Liu, J., Edwards, B., Lv, Z., Cai, R., Liu, Y., Xiao, X., Wang, J., Jiao, F., Wang, R., Huang,
649 X., Guo, B., Sun, J., Zhang, R., Zhang, Y., Tang, K., Zheng, Q., Azam, F., Batt, J., Cai, W.-J.,
650 He, C., Herndl, G.J., Hill, P., Hutchins, D., LaRoche, J., Lewis, M., MacIntyre, H., Polimene,
651 L., Robinson, C., Shi, Q., Suttle, C.A., Thomas, H., Wallace, D., Legendre, L., 2021.
652 Correcting a major error in assessing organic carbon pollution in natural waters. Science
653 Advances 7, eabc7318. https://doi.org/10.1126/sciadv.abc7318
654 Karim, R., Li, S., Su, T., Ayugi, B.O., Babaousmail, H., Xiao, S., 2025. Future Climate Changes
655 on the Qinghai–Tibetan Plateau Under CMIP6 Global Climate Models. International Journal
656 of Climatology e70005. https://doi.org/10.1002/joc.70005
657 Kotlarski, S., Gobiet, A., Morin, S., Olefs, M., Rajczak, J., Samacoïts, R., 2023. 21st Century
658 alpine climate change. Clim Dyn 60, 65–86. https://doi.org/10.1007/s00382-022-06303-3
659 Lan, T., Ma, Q., Lai, Y., Zhang, M., Harbor, J., Luo, X., 2025. Quantifying the water contributions
660 and carbon consequences of permafrost degradation on the Tibetan Plateau. Science Bulletin.
661 https://doi.org/10.1016/j.scib.2025.09.029
662 Li, G., Li, Zongxing, Zhang, B., Li, Zongjie, 2025. Changes in runoff from major alpine
663 watersheds on the Qinghai-Tibetan plateau: A review. Journal of Hydrology: Regional

Studies 60, 102514. https://doi.org/10.1016/j.ejrh.2025.102514

Li, J., Wang, G., Song, C., Sun, S., Ma, J., Wang, Y., Guo, L., Li, D., 2024. Recent intensified erosion and massive sediment deposition in Tibetan Plateau rivers. Nat Commun 15, 722. https://doi.org/10.1038/s41467-024-44982-0

Li, J., Wang, G., Sun, S., Ma, J., Guo, L., Song, C., Lin, S., 2025. Mapping and reconstruct suspended sediment dynamics (1986–2021) in the source region of the Yangtze River, Qinghai-Tibet Plateau using Google Earth Engine. Remote Sensing of Environment 317, 114533. https://doi.org/10.1016/j.rse.2024.114533

Li, L., Wang, T., Yang, J., Yang, H., Tang, L., Yang, D., 2025. Revealing the Long-Term Catchment-Scale Carbon Budget Dynamics on the Permafrost-Dominated Eastern Tibetan Plateau. Global Biogeochemical Cycles 39, e2025GB008743. https://doi.org/10.1029/2025GB008743

Li, M., Peng, C., Zhang, K., Xu, L., Wang, J., Yang, Y., Li, P., Liu, Z., He, N., 2021. Headwater stream ecosystem: an important source of greenhouse gases to the atmosphere. Water Research 190, 116738. https://doi.org/10.1016/j.watres.2020.116738

Li, X., Wang, J., Lin, J., Yin, W., Shi, Y.Y., Wang, L., Xiao, H.B., Zhong, Z.M., Jiang, H., Shi, Z.H., 2022. Hysteresis analysis reveals dissolved carbon concentration – discharge relationships during and between storm events. Water Research 226, 119220. https://doi.org/10.1016/j.watres.2022.119220

Li, Ziliang, Kang, L., Wang, L., Wanek, W., Zhang, D., Wang, G., Lambers, H., Peñuelas, J., Jiang, M., Yang, Y., 2025. Accelerated soil phosphorus cycling upon abrupt permafrost thaw. Nat. Clim. Chang. https://doi.org/10.1038/s41558-025-02445-4

686 Li, Zongjie, Liu, F., Li, H., Liu, M., Li, Zongxing, Feng, Q., Xu, B., Liu, X., 2025. Driving forces
687 of the spatiotemporal supply pattern of runoff in the source region of Yellow River. Journal of
688 Hydrology: Regional Studies 60, 102515. https://doi.org/10.1016/j.ejrh.2025.102515
689 Liu, G., Li, S., Song, K., Wang, X., Wen, Z., Kutser, T., Jacinthe, P.-A., Shang, Y., Lyu, L., Fang,
690 C., Yang, Y., Yang, Q., Zhang, B., Cheng, S., Hou, J., 2021. Remote sensing of CDOM and
691 DOC in alpine lakes across the Qinghai-Tibet Plateau using Sentinel-2A imagery data.
692 Journal of Environmental Management 286, 112231.
693 https://doi.org/10.1016/j.jenvman.2021.112231
694 Liu, H., 2023. Human activity intensity dataset of the Qinghai-Tibet Plateau (2000-2020).
695 National Tibetan Plateau Data Center. https://doi.org/10.3974/geodb.2023.07.08.V1
696 Liu, L., Yang, S., Wang, S., Hu, J., Li, C., Yi, Y., 2025. Influence of the Cascade Reservoir
697 Operation of the Yellow River on the Hydrological Regime of the Main Stream of the Yellow
698 River. Yellow River 47, 42-47+77. https://doi.org/10.3969/j.issn.1000-1379.2025.03.007
699 Liu, P., Zeng, H., Qi, L., Degen, A.A., Boone, R.B., Luo, B., Huang, M., Peng, Z., Qi, T., Wang,
700 W., 2024. Vegetation redistribution is predicted to intensify soil organic carbon loss under
701 future climate changes on the Tibetan Plateau. Science of The Total Environment 932,
702 173034. https://doi.org/10.1016/j.scitotenv.2024.173034
703 Lv, Z., Ran, X., Liu, J., Feng, Y., Zhong, X., Jiao, N., 2024. Effectiveness of Chemical Oxygen
704 Demand as an Indicator of Organic Pollution in Aquatic Environments. Ocean-Land-Atmos
705 Res 3, 0050. https://doi.org/10.34133/olar.0050
706 Ma, M., Wang, Z., Zang, H., Wang, W., Wei, M., Cui, H., 2023. Runoff Simulation and Prediction
707 in the Source Region of the Yellow River Based on SSP Scenarios. Journal of North China

University of Water Resources and Electric Power (Natural Science Edition) 44, 31–40. https://doi.org/10.19760/j.ncwu.zk.2023054

Ma, W., Wu, T., Wu, X., Yang, S., Li, R., Zhou, S., Li, X., Zhu, X., Hao, J., Ni, J., 2023. Carbon budgets and environmental controls in alpine ecosystems on the Qinghai-Tibet Plateau. Catena 229, 107224. https://doi.org/10.1016/j.catena.2023.107224

Maavara, T., Chen, Q., Van Meter, K., Brown, L.E., Zhang, J., Ni, J., Zarfl, C., 2020. River dam impacts on biogeochemical cycling. Nature Reviews Earth & Environment 1, 103–116. https://doi.org/10.1038/s43017-019-0019-0

Maavara, T., Lauerwald, R., Regnier, P., Van Cappellen, P., 2017. Global perturbation of organic carbon cycling by river damming. Nature communications 8, 15347. https://doi.org/10.1038/ncomms15347

Meng, Y., Duan, K., Shi, P., Shang, W., Li, S., Cheng, Y., Xing, L., Chen, R., He, J., 2023. Sensitive temperature changes on the Tibetan Plateau in response to global warming. Atmospheric Research 294, 106948. https://doi.org/10.1016/j.atmosres.2023.106948

Peng, S., 2025a. 1-km monthly precipitation dataset for China (1901-2024). National Tibetan Plateau Data Center. https://doi.org/10.5281/zenodo.3114194

Peng, S., 2025b. 1-km monthly mean temperature dataset for China (1901-2024). National Tibetan Plateau Data Center. https://doi.org/10.11888/Meteoro.tpdc.270961

Regnier, P., Resplandy, L., Najjar, R.G., Ciais, P., 2022. The land-to-ocean loops of the global carbon cycle. Nature 603, 401–410. https://doi.org/10.1038/s41586-021-04339-9

San, M., Jia, S., Yang, C., Liu, J., Yu, Z., Fang, W., Shang, J., Ming, B., Guo, Y., Cheng, L., 2025. Runoff Prediction in the Source Region of the Yellow River Basin Based on the CMIP6

730 Climate Model. Soil and Water Conservation in China 71-77+89.
731 https://doi.org/CNKI:SUN:ZGSB.0.2025-07-020
732 Shang, Y., Wen, Z., Liu, G., Fang, C., Yu, X., Liu, J., Song, K., 2026. Deciphering riverine
733 CODMn sources: driver identification and carbon cycle impacts. Ecological Indicators 190,
734 115312. https://doi.org/10.1016/j.ecolind.2026.115312
735 Vachon, D., Sponseller, R.A., Karlsson, J., 2021. Integrating carbon emission, accumulation and
736 transport in inland waters to understand their role in the global carbon cycle. Global Change
737 Biology 27, 719–727. https://doi.org/10.1111/gcb.15448
738 Wang, L., 2024. Difference and causes of runoff in different sections above Tangnaihai in the
739 source region of the Yellow River. Journal of Qinghai Normal University (Natural Science
740 Edition) 40, 99-104+112. https://doi.org/10.16229/j.cnki.issn1001-7542.2024313
741 Wang, M., Sun, K., Jia, J., Yu, G., Gao, Y., 2026. Unraveling the carbon fraction heterogeneity in
742 China's Rivers: Hydrology, nutrients, and dam regulation. Water Research 288, 124591.
743 https://doi.org/10.1016/j.watres.2025.124591
744 Wang, S., Benoit, G., Raymond, P.A., Yu, G., Zhou, F., Liu, S., Miao, C., Sun, K., Li, Z., Jia, J.,
745 2025. Dissolved carbon storage and flux dynamics in China's inland waters over the past 30
746 years. National Science Review nwaf229. https://doi.org/10.1093/nsr/nwaf229
747 Wang, S., Shen, M., Liu, W., Ma, Y., Shi, H., Zhang, J., Liu, D., 2022. Developing remote sensing
748 methods for monitoring water quality of alpine rivers on the Tibetan Plateau. GIScience &
749 Remote Sensing 59, 1384–1405. https://doi.org/10.1080/15481603.2022.2116078
750 Wang, T., Yang, D., Yang, Y., Piao, S., Li, X., Cheng, G., Fu, B., 2020. Permafrost thawing puts
751 the frozen carbon at risk over the Tibetan Plateau. Science Advances 6, eaaz3513.

https://doi.org/10.1126/sciadv.aaz3513

Wang, W., Zhong, J., Li, S.-L., Ulloa-Cedamanos, F., Xu, Sen, Chen, S., Lai, M., Xu, Sheng, 2023. Constraining the sources and cycling of dissolved inorganic carbon in an alpine river, eastern Qinghai-Tibet Plateau. Science of The Total Environment 901, 166262. https://doi.org/10.1016/j.scitotenv.2023.166262

Wang, X., Wu, Y., Luo, M., Katsanou, K., Wenninger, J., Bol, R., 2025. Exports of organic matter, phosphorus and nitrogen from Sichuan Basin: A critical region regulating water quality of the Upper Yangtze River, China. Journal of Hydrology 662, 133889. https://doi.org/10.1016/j.jhydrol.2025.133889

Wen, W., Gao, L., Cheng, H., Xiao, L., Zhang, S., Li, S., Jiang, X., Xia, X., 2024. Legacy and alternative perfluoroalkyl acids in the Yellow River on the Qinghai-Tibet Plateau: Levels, spatiotemporal characteristics, and multimedia transport processes. Water Research 262, 122095. https://doi.org/10.1016/j.watres.2024.122095

Wu, Y., Su, H., Cheng, L., Qin, S., Zou, K., Liu, Y., Zhou, J., Liu, P., Zhang, L., 2024. Exploring hydrological controls on dissolved organic carbon export dynamics in a typical flash flood catchment using a process-based model. Science of The Total Environment 921, 171139. https://doi.org/10.1016/j.scitotenv.2024.171139

Xu, S., Li, S.-L., Bufe, A., Klaus, M., Zhong, J., Wen, H., Chen, S., Li, L., 2024. Escalating Carbon Export from High-Elevation Rivers in a Warming Climate. Environ. Sci. Technol. 58, 7032–7044. https://doi.org/10.1021/acs.est.3c06777

Yan, N., Qiu, Z., Zhang, C., Yan, Y., Liu, D., 2025. Landsat monitoring reveals the history of river organic pollution across China during 1984–2023. Water Research 275, 123210.

https://doi.org/10.1016/j.watres.2025.123210

Yan, Y., Lauerwald, R., Wang, X., Regnier, P., Ciais, P., Ran, L., Gao, Y., Huang, L., Zhang, Y., Duan, Z., 2023. Increasing riverine export of dissolved organic carbon from China. Global Change Biology 29, 5014–5032. https://doi.org/10.1111/gcb.16819

Yang, J., Wang, T., Yang, D., Yang, Y., 2023. Insights into runoff changes in the source region of Yellow River under frozen ground degradation. Journal of Hydrology 617, 128892. https://doi.org/10.1016/j.jhydrol.2022.128892

Yang, M., Li, S., Wang, S., Huang, Q., Shen, Q., Kang, Y., Shi, M., Zhang, Y., Luo, D., 2025. Latitudinal gradient and environmental drivers of soil organic carbon in permafrost regions of the Headwater Area of the Yellow River. Carbon Neutrality 4, 16. https://doi.org/10.1007/s43979-025-00130-1

Yao, T., Bolch, T., Chen, D., Gao, J., Immerzeel, W., Piao, S., Su, F., Thompson, L., Wada, Y., Wang, L., Wang, T., Wu, G., Xu, B., Yang, W., Zhang, G., Zhao, P., 2022. The imbalance of the Asian water tower. Nat Rev Earth Environ 3, 618–632. https://doi.org/10.1038/s43017-022-00299-4

Zeng, F., Song, C., Cao, Z., Xue, K., Lu, S., Chen, T., Liu, K., 2023. Monitoring inland water via Sentinel satellite constellation: A review and perspective. ISPRS Journal of Photogrammetry and Remote Sensing 204, 340–361. https://doi.org/10.1016/j.isprsjprs.2023.09.011

Zhang, Z., Zhang, L., Liu, Y., Jin, M., 2024. Responses of annual streamflow variability to annual precipitation, extreme climate events and large-scale climate phenomena in the Qinghai-Tibet Plateau. Journal of Hydrology 632, 130969. https://doi.org/10.1016/j.jhydrol.2024.130969

Zhao, W., Cheng, Y., Jian, J., Jiao, J., Cheng, C., Li, J., Chen, T., 2023. Water erosion changes on

the Qinghai-Tibet Plateau and its response to climate variability and human activities during 1982–2015. CATENA 229, 107207. https://doi.org/10.1016/j.catena.2023.107207

Zhi, W., Appling, A.P., Golden, H.E., Podgorski, J., Li, L., 2024. Deep learning for water quality. Nat Water 2, 228–241. https://doi.org/10.1038/s44221-024-00202-z